Mineralogical Magazine, October 2015, Vol. 79(5), pp. 1159–1173

Crystal structure, thermal behaviour and parageneses of koninckite, $FePO_4 \cdot 2.75H_2O$

J. Plášil[1,*], J. Majzlan[2], M. Wierzbicka-Wieczorek[2] and B. Kiefer[3]

[1] Institute of Physics ASCR, v.v.i., Na Slovance 2, Prague 8, 182 21, Czech Republic
[2] Institute of Geosciences, Burgweg 11, University of Jena, D-07749, Germany
[3] Department of Physics, 1255 N Horseshoe, New Mexico State University, Las Cruces, New Mexico, 88003, USA

[*Received 3 July 2014; Accepted 1 February 2015; Associate Editor: I. Graham*]

ABSTRACT

The crystal structure of the mineral koninckite was solved from synchrotron powder X-ray diffraction (XRD) data and refined using density-functional theory (DFT) calculations. Koninckite is tetragonal, with the space group $P4_12_12$, $a = 11.9800(5)$ Å, $c = 14.618(1)$ Å, $V = 2097.9(2)$ Å^3, $Z = 8$. Its structure is a heteropolyhedral framework with zeolite-like tunnels along [001]. Owing to the severe peak overlap in the powder XRD data and the probable intergrowth of enantiomorphic domains in koninckite, the DFT calculations were applied to provide precise atomic positions (including hydrogen). Additionally, the DFT calculations suggest strongly that koninckite is an antiferromagnetic semiconductor, at least at low temperatures. The DFT computations were used to locate H_2O molecules in the channels and to complete the structural description. Thermogravimetric analysis and powder XRD data at variable temperatures show that the structure of koninckite dehydrates and eventually collapses between 160–180°C. Negative thermal expansion was observed between 80 and 150°C. A list of the known occurrences of koninckite suggests that this mineral is not as rare as assumed previously; koninckite is often fine-grained, inconspicuous, and thereby easy to overlook. Koninckite is yet another natural example of an Fe-phosphate zeolitic material.

Keywords: koninckite, ferric phosphate, synchrotron diffraction, crystal structure, density-functional theory.

Introduction

Koninckite is seemingly an uncommon ferric phosphate, related chemically to heterosite ($FePO_4$) and phosphosiderite ($FePO_4 \cdot 2H_2O$). Since its first description (Cesàro, 1884) (Fig. 1*a*), this mineral has been detected at a number of localities (see below). The long list of occurrences, together with its fine-grained and inconspicuous nature, suggests that koninckite is not a particularly rare mineral and can form commonly in environments enriched in ferric iron and phosphate. Because of the small grain size, the crystal structure of this mineral was unresolved.

The structures of phosphates of ferric iron are of a broad interest. The strongly preferred association of phosphate with ferric iron in natural and man-made settings has been recognized for a long time, for example, the strong adsorption of phosphate onto the surface of ferrihydrite (e.g. Wang *et al.*, 2013). Precipitating ferrihydrite incorporates phosphate into nuclei of poorly ordered ferric phosphate (Voegelin *et al.*, 2010) and amorphous ferric phosphates constitute bacterioferritins (e.g. Michel *et al.*, 2010). The crystalline Fe phosphates can thus serve as model structures for the exploration of the atomic arrangement in poorly-ordered systems with similar chemistry.

In this contribution, we present the crystal structure of koninckite, discuss the behaviour of the phase as a function of temperature, and draw conclusions from the published parageneses of the mineral. The structure was partially solved from powder X-ray diffraction data. The inherent limitations associated with the X-ray diffraction data (severe peak overlap), the possibility of

* E-mail: plasil@fzu.cz
DOI: 10.1180/minmag.2015.079.5.10

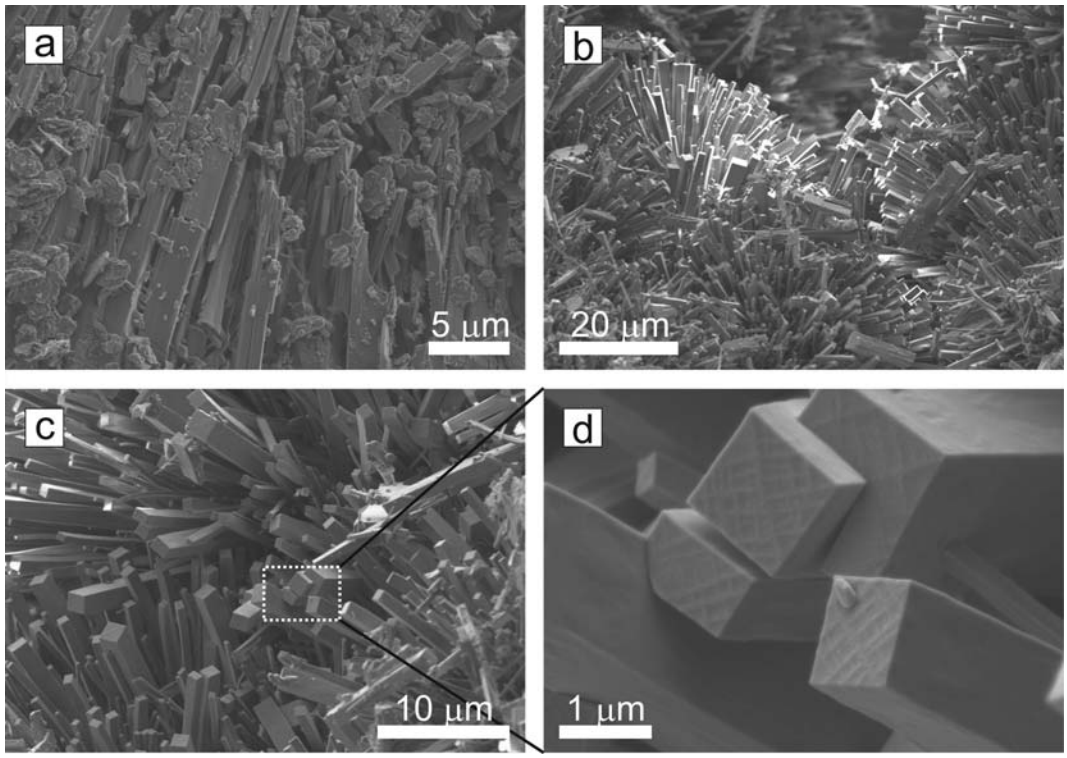

FIG. 1. Scanning electron microphotographs of the koninckite crystals: (*a*) from the type locality Visé in Belgium, with flakes of clay minerals; (*b*,*c*,*d*) from Kociha, Rimavská Sobota (Slovakia).

enantiomorphic space groups, and the location of hydrogen in network forming H_2O and extra-framework H_2O hinders a complete experimental structure refinement of koninckite. Therefore, we augmented our X-ray diffraction observations with first-principles density-functional theory (DFT) computations to obtain the complete crystallographic description of koninckite.

Materials and methods

The natural sample used for this study originated from Kociha, near Rimavská Sobota in Slovakia (Novák *et al.*, 2003) and consisted of large (several cm) quartz crystals with a sprinkling of pale pink globular aggregates of koninckite (size of the aggregates ~1 mm). The acicular crystals of koninckite (Fig. 1*b*,*c*,*d*) are barely visible under a microscope and the crystallite size was too small for single-crystal XRD data, even at a synchrotron.

The *in situ* variable-temperature XRD patterns were collected using a Bruker D8 Advance diffractometer, equipped with a Cu X-ray source operated at 40 kV and 40 mA, a fixed divergence slit at 0.1°, a soller slit at 2.5° and a Lynx-Eye detector. The temperature stage was a Model CHC+ Plus Cryo & Humidity Chamber (Anton-Paar GmbH, Graz, Austria) fitted with a platinum heater. A Pt 100 temperature sensor was integrated in the sample holder for accurate measurement and control of the temperature. The *in situ* diffraction data were collected from 20° to 300°C with a temperature step of 20°C. The XRD patterns were measured from 5° to 60°2θ, with a step of 0.02°2θ and counting time of 2.5 s per point.

Powder XRD patterns used for indexing and structure solution were collected at the bending-magnet beamline PDIFF at the synchrotron light source ANKA (Angströmquelle Karlsruhe, Germany). X-rays of wavelength of 0.69244(1) Å were selected by a double crystal Si(111) monochromator. The wavelength and the zero angle of the diffractometer were determined with silicon powder (NIST standard reference material 640). The sample was loaded into a 1.0 mm glass

https://doi.org/10.1180/minmag.2015.079.5.10 Published online by Cambridge University Press

capillary which was rotated about its axis during data collection. The intensity of the incoming beam was monitored during data collection by an ion chamber and the measured intensities of the diffracted beam were corrected for the decay and fluctuations of the primary beam. The XRD patterns were collected at room temperature, over an angular range of 0.9 to 19.7° in 2θ, with a step of 0.005° and counting time of 1 s per point.

The initial indexing of the powder diffraction data was performed with the program *Crysfire* (Shirley, 2000). The LeBail decomposition was performed using the crystallographic suite *Jana2006* (Petříček *et al.*, 2006, 2014) and the structure was solved from the powder data using a charge-flipping algorithm (Oszlányi and Sütő, 2004, 2008; Palatinus, 2013) implemented in the program *Superflip* (Palatinus and Chapuis, 2007). The bond-valence calculations were carried out following the approach of Brown (2002).

Thermogravimetric and differential thermal analysis (TGA/DTA) were performed with a Netzsch 449 system in corundum crucibles, in argon flow (40 ml/min), with a heating rate of 10 K/min. For the electron microscopy work, selected hand-picked fragments of the samples were carbon-coated. The images and energy-dispersive analyses were acquired with a field-emission gun scanning electron microscope (SEM) Zeiss Ultra Plus (Friedrich-Schiller University Jena, Germany) with an accelerating voltage of 15 kV.

The DFT computations were performed subject to periodic boundary conditions as implemented in *VASP* (Kresse and Furthmuller, 1996*a*,*b*). Ion-valence electron interactions were described using all-electron-like projector augmented wave (PAW) potentials (Blöchl, 1994; Kresse and Joubert, 1999) where Fe (4s3d), P (3p), O(2s), H(1s) atomic electron configurations were treated as valence electrons. Electronic exchange and correlation effects were described within the generalized gradient approximations (GGA) in the PBE parametrization (Perdew *et al.*, 1996), including spin interpolation by Vosko *et al*. (1980). All geometry optimizations were performed using a planewave cut-off energy of $E_{cut} = 500$ eV using a single k-point (Γ-point). The Fermi level was broadened slightly using the Methfessel-Paxton technique (Methfessel and Paxton, 1989) with $\sigma = 0.1$ eV. All computations were spin-polarized in order to allow for non-trivial magnetic ground states in koninckite. The initial geometry for the geometry optimizations was obtained from the powder diffraction refinement (space group $P4_12_12$) and undersaturated polyhedral oxygen atoms were saturated with hydrogen to ensure a charge neutral crystallographic unit cell (O7–O10, see below). All relaxations were conducted in a symmetry preserving mode unless noted otherwise. Increasing E_{cut} to 600 eV shows that energies are converged to within 1.1 meV/atom. Similarly, a finer Γ-centred $2 \times 2 \times 2$ k-point grid shows that energies are converged to within 0.5 meV/atom. Relaxed lattice parameters are converged to within 0.2% and the volume to within 0.6%, respectively. Moreover, the magnetic structure remains unchanged. The antiferromagnetic structure was generated by placing spin-up and spin-down Fe atoms on the crystallographic Fe(1) and Fe(2) sites, respectively. This partitioning of spin-up and spin-down Fe is consistent with the crystallographic space group. Thermal effects have been ignored following previous work on similar compounds (Majzlan and Kiefer, 2006).

Results

Crystal morphology

As mentioned above, the koninckite crystals available to us were too small for a single-crystal study, although the material we had was well crystalline. The euhedral crystals (Figs 1*b*,*c*,*d*) consist of a combination of a tetragonal prism and a pinacoid. The basal faces show a peculiar pattern on a submicrometre scale (Fig. 1*d*) and it could be speculated that the ridges signify boundaries between structural domains that belong to the inversely oriented domains arising from the enantiomorphic space group $P4_12_12$.

Crystal structure: X-ray diffraction

Indexing of the powder XRD pattern confirmed the tetragonal symmetry (Table 1), as proposed by van Tassel (1968). The space group was then determined by *Superflip*, deciphering the symmetry operators from the flipped electron density (Palatinus and van der Lee, 2008) as an enantiomorph tetragonal space group $P4_12_12$ or $P4_32_12$. Repeated runs of the structure solution (20 runs) showed a higher frequency of the $P4_12_12$ space-group assignments (in 14 cases), which was then used successfully in the subsequent Rietveld refinement using the *Jana2006* software package. The electron density obtained from the solution and the interpretation of the positive electron density peaks by the *Jana2006* program

https://doi.org/10.1180/minmag.2015.079.5.10 Published online by Cambridge University Press

TABLE 1. Details for crystallography, data collection and Rietveld refinement of koninckite.

Koninckite (powder X-ray diffraction data), $FePO_{6.75}$	
a [Å]	11.9800(3)
c [Å]	14.6178(8)
V [Å^3]	2097.96(14)
Z	16
Space group	$P4_12_12$
$D_{calc.}$ [g.cm^{-3}]	2.467(1) (applicable for the summary composition given above)
Data collection	Synchrotron, ANKA
Temperature	293 K
Source, wavelength	PDIFF, 0.69244 Å
Specimen	Powder in 0.64 mm glass capillary
Collection mode	Rotation along φ axis
Limiting θ angles	0.65–39.00°
No. of points; observed reflections	7501; 588 [$I_{obs} > 3\sigma(I)$]
Absorption correction (mm^{-1}), type	2.81, cylindrical sample
F_{000}	1520
Rietveld refinement by *Jana2006*	
Parameters, reflections, restraints, constraints	75, 0, 13
R_p, wR_p, R_{exp}	0.0890, 0.1142, 0.0405
Goof	2.82
R_F, wR_F (obs)	0.0513, 0.0621
R_{Bragg}, wR_{Bragg}	0.0807, 0.1262
$\Delta\rho_{min}$, $\Delta\rho_{max}$ (e Å^{-3})	–0.53, 0.51
Weighting scheme	σ

provided an almost complete structure model for the 3D framework of Fe-based octahedra interconnected by PO_4 tetrahedra. For the subsequent refinement, the Marquardt technique of damping the least-squares refinement was used to reach a smoother convergence of the fit. By adding several O atoms, the heteropolyhedral framework was completed. However, the bond lengths within the polyhedra as obtained from Rietveld refinements showed unexpected and anomalous variations, and were even inferior (in terms of bond lengths and angles) to the initial model obtained from the structure solution. This is not too surprising for structure refinements of complex materials from powder XRD data, but substantial improvement was obtained when the cylindrical absorption correction implemented in the *Jana2006* algorithm was applied during the refinement (the decrease in R_p was ~3%). In the final steps of the refinement, all O atoms, including the ones localized in the channels of the structure (see below), were located by the difference Fourier technique and the location of extra-framework O positions were refined. The final indices of agreement against powder data were $R_p = 8.90\%$, $wR_p = 11.42\%$, $R_F = 5.17\%$ (against 588 observed peaks) and $R_{Bragg} = 8.07\%$ (Table 1). The data and the final fit are shown in Fig. 2. The largest difference Fourier peaks were 0.51 and –0.53 e Å^{-3}. The final atomic coordinates obtained from the Rietveld refinement are listed in Table 2. Selected bond lengths derived from the Rietveld refinement are listed in Table 3.

The structure of koninckite contains two Fe, two P and 14 O sites in the asymmetric unit that were found using the solution from the synchrotron powder diffraction data (Table 2). Iron atoms are sixfold-coordinated, each by four O atoms and two H_2O groups. They are linked to each other by sharing vertices with two PO_4 tetrahedra of the P2 atoms (generated by symmetry) (Fig. 3), which are oriented *up-down* respectively to each other. The octahedral–tetrahedral linkage extends into a 3-dimensional (zeolite-like) framework (Fig. 4) with pronounced channels – voids running parallel to the [001] direction. Bond-valence analysis as well as charge-balance requirements indicate that all Fe in the structure is trivalent and P is pentavalent. According to the calculated bond-valence sums, the atoms O7, O8, O9, O10, O13 and O14 belong to H_2O groups. Four of them (O7–O10) represent apical atoms of the FeO_6 octahedra and point inside the channels of the structure. Atoms O13 and O14 belong to extra-framework H_2O that are bonded by hydrogen bonds only.

Based on the results of the Rietveld refinement, the structural formula of koninckite is $Fe_2(PO_4)_2(H_2O)_{5.5}$, for $Z = 8$, or simply $Fe(PO_4)(H_2O)_{2.75}$ for $Z = 16$. Both formulae differ from the generally accepted formula of koninckite of $Fe_2(PO_4)_2(H_2O)_6$ (for $Z = 8$), however, no additional O atoms within the channel and the structure could be identified. Therefore, we conclude that the most acceptable formula of koninckite is $Fe(PO_4)(H_2O)_{2.75}$ ($Z = 16$).

Crystal and magnetic structure: computational results

The relaxed lowest energy structure of $Fe_2(PO_4)_2(H_2O)_4$ corresponds to an antiferromagnetic (afm) arrangement, which is ~2.7 meV/atom more stable than the corresponding ferromagnetic (fm)

https://doi.org/10.1180/minmag.2015.079.5.10 Published online by Cambridge University Press

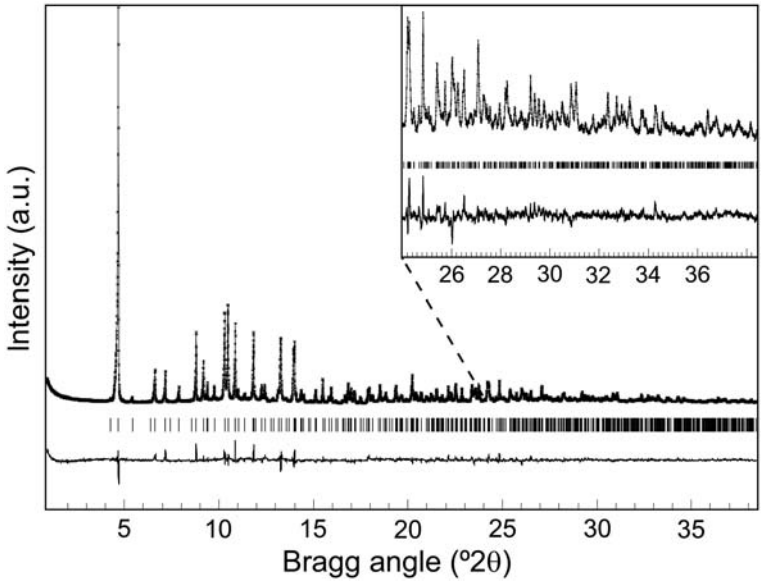

FIG. 2. Final plot from the Rietveld refinement of the koninckite structure.

arrangement. The analysis of the site-projected spin-density reveals that only the Fe ions possess significant magnetic moments (magnitude larger than m = 4 μ_B/Fe atom), as expected. Furthermore, the electronic density of states (eDOS) shows that koninckite is a semiconductor. The oxidation state of Fe can be inferred from the crystal chemistry: Each Fe is coordinated by four bridging oxygen atoms to PO_4 tetrahedra and two framework H_2O molecules. Removing one H_2O molecule or eight crystallographically equivalent H_2O molecules is endothermic and requires ~0.4 eV/H_2O but leaves the magnetic state unchanged. This finding suggests strongly that the origin of the magnetism must be attributed to the presence of bridging Fe–O–P units. Furthermore, pentavalent P donates 1.25e to each of the four coordinating bridging oxygen atoms, the remaining 0.75e needed by oxygen to attain its formal valence charge (–2) are contributed by Fe. Thus, Fe is trivalent and the high magnitudes of the site-projected magnetic moments of Fe suggest strongly a high-spin state. It is well-known that DFT is insufficient to describe the electronic and magnetic structure of some 3*d* transition metal oxides such as FeO (Mazin *et al.*, 1998; Schrön *et al.*, 2012), Fe_2O_3 (Punkkinen *et al.*, 1999; Rollmann *et al.*, 2004) and Fe_3O_4 (Wenzel and Steinle-Neumann, 2007; Bengtson *et al.*, 2013). In order to test the stability of the electronic and magnetic structure, we performed DFT+U computations (Dudarev *et al.*, 1998) using U–J = 4 eV, similar to previous computations on Fe_xO_y. The bandgap increases from 1.2 eV (DFT) to 2.4 eV (DFT+U) but the magnetic structure remains unaffected. Thus, the magnetic structure as obtained from the DFT computations is corroborated and the $FePO_4{\cdot}2H_2O$ framework structure of koninckite is predicted to be an antiferromagnetic semiconductor with trivalent Fe in a (local) high-spin state, at least at low temperatures.

The relaxed nuclear crystal structures of the afm and fm are almost identical (Table 2). The average FeO_6 bond lengths are 2.028 Å and 2.029 Å for afm and fm configurations, respectively (Table 3). Similarly, the PO_4 bond lengths are almost identical, 1.549 Å and 1.550 Å for afm and fm, respectively. The computed bond lengths compare favourably with the expected bond lengths as inferred from the ionic radii, 2.00 Å and 1.52 Å for FeO_6 and PO_4, respectively. The observation that the Fe–O bond length are slightly larger than expected is attributed to the observation that the GGA tends to overestimate lattice parameters (Holzwarth *et al.*, 1997). As expected, the orientation of the spins on Fe has only a very small effect on the crystal chemistry as in both cases Fe is in a high-spin state with identical coordination environments. The average O–H bond length of the framework H_2O molecules needed for charge neutrality ranges from 0.974 Å to 1.010 Å with an average of 0.995 Å (Table 4), close to the

https://doi.org/10.1180/minmag.2015.079.5.10 Published online by Cambridge University Press

TABLE 2. Atomic coordinates in the asymmetric unit of koninckite. All atoms occupy the Wyckoff 8*b* sites, except O14 (4*a*).

	Rietveld refinement			DFT calculations antiferromagnetic structure			DFT calculations ferromagnetic structure		
	x/a	*y/b*	*z/c*	*x/a*	*y/b*	*z/c*	*x/a*	*y/b*	*z/c*
Fe1	0.4057(11)	0.1531(12)	0.0972(10)	0.3442	0.0980	0.4020	0.3446	0.0981	0.4019
Fe2	0.3712(12)	−0.1935(11)	−0.0799(10)	0.1959	0.3780	0.1663	0.1958	0.3782	0.1662
P1	0.374(2)	0.170(2)	0.3232(19)	0.3297	0.1346	0.1737	0.3298	0.1348	0.1735
P2	0.376(2)	0.077(2)	−0.1193(19)	0.1226	0.4226	0.3829	0.1228	0.4228	0.3829
O1	0.534(4)	−0.170(4)	−0.110(4)	0.3721	0.0432	0.0977	0.3272	0.0435	0.0974
O2	0.383(4)	−0.198(4)	0.051(3)	0.1996	0.3797	0.3045	0.2004	0.3801	0.3047
O3	0.333(4)	−0.054(4)	−0.093(3)	0.0377	0.3326	0.1648	0.0376	0.3321	0.1653
O4	0.283(4)	0.267(4)	0.345(3)	0.2304	0.2144	0.1570	0.2301	0.2142	0.1568
O5	0.438(4)	−0.022(4)	0.100(4)	0.0018	0.4325	0.3490	0.0023	0.4332	0.3486
O6	0.449(5)	0.182(4)	0.230(3)	0.3166	0.0767	0.2676	0.3170	0.0768	0.2674
O7	0.399(4)	−0.350(4)	−0.073(3)	0.3692	0.4152	0.1619	0.3691	0.4152	0.1618
O8	0.245(4)	0.136(5)	0.121(3)	0.3763	0.2693	0.3735	0.3766	0.2693	0.3737
O9	0.373(4)	−0.209(4)	−0.226(3)	0.1994	0.3719	0.0269	0.1994	0.3721	0.0270
O10	0.375(4)	0.318(4)	0.085(3)	0.1725	0.1344	0.4035	0.1731	0.1348	0.4034
O11	0.441(4)	−0.184(4)	−0.409(4)	0.4399	0.2019	0.1694	0.4398	0.2024	0.1693
O12	0.362(4)	0.156(4)	−0.035(3)	0.1339	0.3390	0.4635	0.1332	0.3387	0.4633
O13	0.111(5)	–0.039(5)	0.029(4)	0.0315	0.1401	0.2583	0.0318	0.1398	0.2586
O14	0.613(5)	–0.387(5)	0	0.1131	0.1131	0	0.1129	0.1129	0
H1	NA	NA	NA	0.4143	0.3465	0.1731	0.4141	0.3465	0.1730
H2	NA	NA	NA	0.3853	0.4742	0.2078	0.3852	0.4742	0.2077
H3	NA	NA	NA	0.4185	0.3130	0.4193	0.4192	0.3131	0.4193
H4	NA	NA	NA	0.3115	0.3142	0.3511	0.3120	0.3144	0.3511
H5	NA	NA	NA	0.3428	0.1310	0.0033	0.3428	0.1311	0.0034
H6	NA	NA	NA	0.2034	0.4507	0.0025	0.2032	0.4509	0.0025
H7	NA	NA	NA	0.1528	0.2089	0.4302	0.1532	0.2093	0.4301
H8	NA	NA	NA	0.1324	0.1317	0.3438	0.1328	0.1317	0.3438
H9	NA	NA	NA	0.0415	0.0787	0.2154	0.0418	0.0783	0.2157
H10	NA	NA	NA	0.0416	0.2097	0.2211	0.0416	0.2094	0.2212
H11	NA	NA	NA	0.1455	0.1523	0.0534	0.1451	0.1522	0.0534

TABLE 3. Comparison of selected interatomic distances for the koninckite structure obtained from Rietveld refinement of the powder diffraction data and DFT calculations.

Rietveld		DFT (afm)		DFT (fm)	
Fe1–O8	1.97	Fe1–O8	2.129	Fe1–O8	2.126
Fe1–O12	2.00	Fe1–O12	2.013	Fe1–O12	2.017
Fe1–O6	2.04	Fe1–O6	2.009	Fe1–O6	2.010
Fe1–O10	2.02	Fe1–O10	2.103	Fe1–O10	2.101
Fe1–O11	1.88	Fe1–O11	1.989	Fe1–O11	1.995
Fe1–O5	2.13	Fe1–O5	1.923	Fe1–O5	1.926
<Fe1–O>	2.01	<Fe1–O>	2.027	<Fe1–O>	2.029
σ^2	50.04	σ^2	20.67	σ^2	20.76
Fe2–O1	2.009	Fe2–O1	2.008	Fe2–O1	2.009
Fe2–O2	1.92	Fe2–O2	2.020	Fe2–O2	1.974
Fe2–O3	1.74	Fe2–O3	1.972	Fe2–O3	2.025
Fe2–O4	1.92	Fe2–O4	2.009	Fe2–O4	2.001
Fe2–O7	1.91	Fe2–O7	2.125	Fe2–O7	2.124
Fe2–O9	2.14	Fe2–O9	2.039	Fe2–O9	2.037
<Fe2–O>	1.94	<Fe2–O>	2.029	<Fe2–O>	2.030
σ^2	50.08	σ^2	18.78	σ^2	19.33
P1–O1	1.47	P1–O1	1.560	P1–O1	1.561
P1–O4	1.63	P1–O4	1.546	P1–O4	1.547
P1–O6	1.64	P1–O6	1.546	P1–O6	1.546
P1–O11	1.53	P1–O11	1.548	P1–O11	1.548
<P1–O>	1.57	<P1–O>	1.550	<P1–O>	1.550
σ^2	66.17	σ^2	1.46	σ^2	1.63
Δ	0.042	Δ	0.003	Δ	0.003
P2–O5	1.32	P2–O5	1.534	P2–O5	1.534
P2–O12	1.56	P2–O12	1.553	P2–O12	1.553
P2–O3	1.70	P2–O3	1.551	P2–O3	1.552
P2–O2	1.54	P2–O2	1.559	P2–O2	1.559
<P2–O>	1.53	<P2–O>	1.549	<P2–O>	1.550
σ^2	21.04	σ^2	3.81	σ^2	3.64
Δ	0.070	Δ	0.005	Δ	0.005

Polyhedral geometry measures: σ^2 – bond-angle variance (Robinson *et al.*, 1971); Δ – bond-length distortion index (Brown and Shannon, 1973).

average O–H bond length as derived from neutron diffraction for H_2O-bearing compounds, 1.0 Å. (e.g. Majzlan *et al.*, 2010). The hydrogen-bond network (Fig. 5) and the calculated bond valences, when including the H atoms, provide an excellent description of the crystal structure and indicate bonding saturation for all atoms in the structure.

The computations also predict that extra-framework water is likely to be present in koninckite. Placing 8 H_2O molecules on 8*a* positions in space group $P4_12_12$ and evaluating the energetics for water uptake from: $FePO_4{\cdot}2H_2O + H_2O(g) \Leftrightarrow FePO_4{\cdot}2.5H_2O$ shows that the reaction is exothermic by –0.7 eV/H_2O. Similarly, adding 8 more H_2O molecules on 8*a* positions leading to $FePO_4{\cdot}3H_2O$ is also found to be exothermic by –0.6 eV/H_2O. The effect of water uptake on the crystal structure is small, the relaxed cell volume is 2155.2 Å^3 (a = 12.062 Å, c = 14.813 Å), ~0.3% lower than the unit cell without extra-framework H_2O. Adding eight additional H_2O molecules leads to a ~3% increase of the unit-cell volume which is attributed to the larger electrostatic repulsion as the H_2O content in the channels increases. As expected, extra-framework H_2O is too weakly bound to affect the much stronger FeO_6/PO_4 bonds in the

https://doi.org/10.1180/minmag.2015.079.5.10 Published online by Cambridge University Press

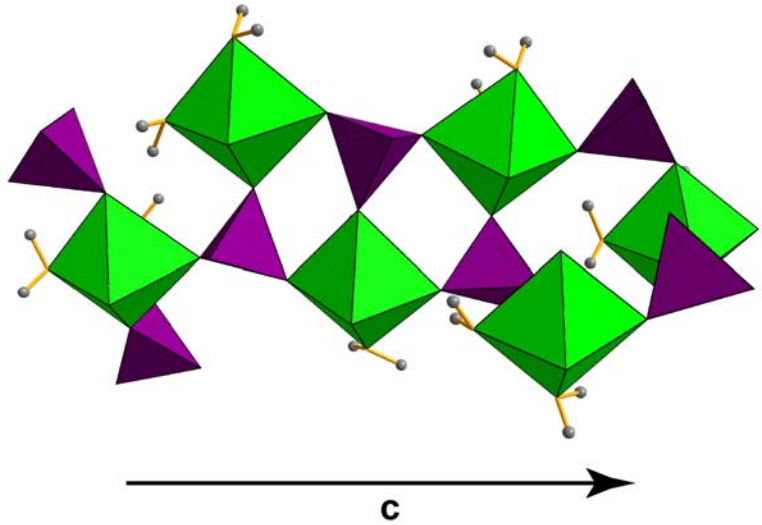

FIG. 3. A fragment of the structure of koninckite, projection approximately onto [110]. This view shows the alternating phosphate tetrahedra and $Fe(O,H_2O)_6$ octahedra in the complex heteropolyhedral chains which build the walls of the zeolite-like structure.

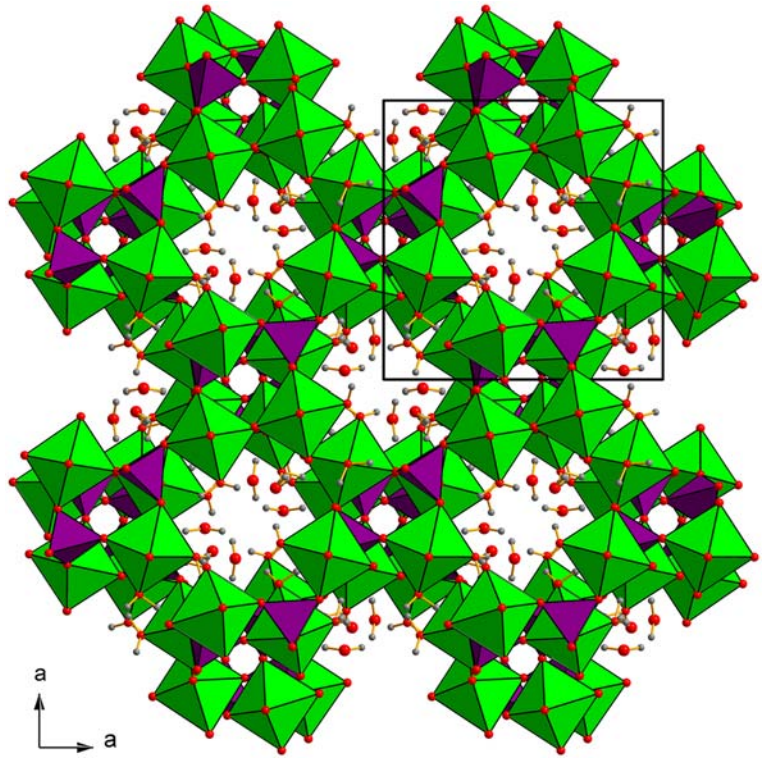

FIG. 4. Projection of the crystal structure of koninckite onto [001]. The tunnels in the structure are filled with H_2O molecules, not shown here. The square shows the unit cell.

https://doi.org/10.1180/minmag.2015.079.5.10 Published online by Cambridge University Press

TABLE 4. Hydrogen-bond geometry for koninckite obtained from the DFT calculations (antiferromagnetic structure).

	D–H	H···*A*	<*D*–H···*A*>
O7–H1···O12	0.997	1.761	154.31
O7–H2···O14	0.993	1.776	154.67
O8–H3···O13	0.989	1.808	160.74
O8–H4···O2	0.999	1.696	173.86
O9–H5···O1	0.994	1.744	152.42
O9–H6···O6	1.010	1.556	164.87
O10–H7···O12	1.003	1.649	171.54
O10–H8···O13	0.997	1.742	163.92
O13–H9···O7	0.974	2.905	165.16
O13–H10···O3	1.003	1.688	170.65
O14–H11···O4 (2×)	0.990	1.970	170.89

D – donor, *A* – acceptor

3-dimensional heteropolyhedral framework structure. Furthermore, we find that the magnetic and electronic properties of the zeolite-like framework remain unaffected by extra-framework water.

Thermal analysis and the structure as a function of temperature

Thermogravimetric analysis shows a relatively simple behaviour of koninckite upon heating. The sample studied loses water continually between 25 and 300°C, without discernible separate thermal events (Fig. 6).

Variable-temperature XRD data show that the structure of koninckite holds up to 160–180°C. In this temperature interval, most of the koninckite peaks disappear and the elevated background indicates that the samples became amorphous. These observations can be interpreted as a loss of the extra-framework water up to 160–180°C and subsequent dehydration of the framework, associated with the collapse of the zeolite-like structure of koninckite. The lattice parameters of koninckite show a peculiar trend (Fig. 7, Table 5). Initially, the structure is slowly expanding with the temperature increase, as expected. At 80°C, the expansion reaches its maximum and the structure begins to collapse. The negative thermal expansion (NTE) seen between 80 and 150°C may be related to water loss from the tunnels in the structure. During the NTE, both lattice parameters *a* and *c* decrease simultaneously (Fig. 7*b*). The decrease of *c*, however, begins at 40°C, but *a* first starts decreasing at 80°C. There are also differences in the magnitude of the decrease; the decline in *c* is larger (0.35 Å) than the decline in *a* (0.18 Å). Before the final amorphization, the structure suddenly expands at 160°C. We must note, however, that the lattice parameters for koninckite at 160°C had uncertainties about three times greater than the uncertainties at the lower temperatures. Despite these greater uncertainties, the expansion before the final collapse seems to be well-documented by the experiments. We assume that this behaviour is related to the step-wise loss of H_2O molecules, although the TGA data, as mentioned above, show a continuous water loss. The DFT computations predict that framework H_2O is bound by ~0.4 eV/H_2O while extra-framework water is predicted to be bound by ~0.6–0.7 eV/H_2O. These similar energies are consistent with the TGA analysis and a step-wise loss of H_2O.

Discussion

Similar minerals and synthetic phases

Several ferric phosphate minerals are known (see Huminicki and Hawthorne, 2002). In terms of their structure, they are typical by their heteropolyhedral networks built by $Fe(O,OH,OH_2)_6$ octahedra and phosphate tetrahedra. Minerals that are chemically similar to koninckite are heterosite ($FePO_4$) and phosphosiderite ($FePO_4 \cdot 2H_2O$). Their structures are dense networks, heterosite has the olivine-type structure (Eventoff *et al.*, 1972), phosphosiderite is

https://doi.org/10.1180/minmag.2015.079.5.10 Published online by Cambridge University Press

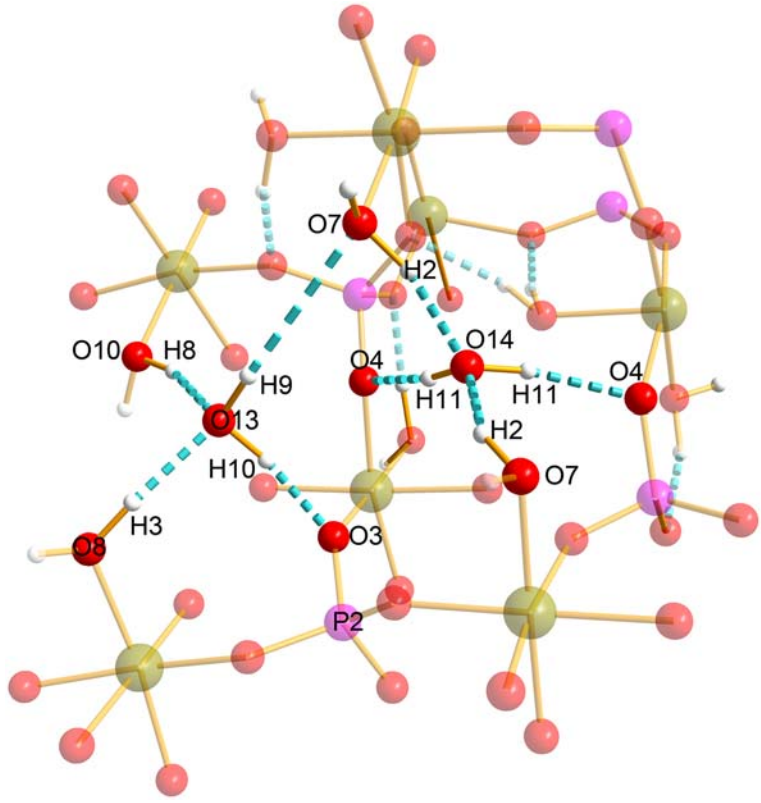

FIG. 5. Hydrogen bonds between the H_2O13 and H_2O14 molecules and the zeolitic framework of koninckite.

isostructural with the Al phosphate metavariscite (Kniep and Mootz, 1973).

Structurally, greater similarity to koninckite is found in beraunite $[Fe^{2+}Fe^{3+}_5(PO_4)_4(OH)_5(H_2O)_6]$ (Fanfani and Zanazzi, 1967; Moore and Kampf, 1992) and cacoxenite $[Fe_{25}(PO_4)_{17}O_6(OH)_{12}(H_2O)_{75}]$ (Moore and Shen, 1983). Both of these minerals are characterized by an open, zeolite-like framework,

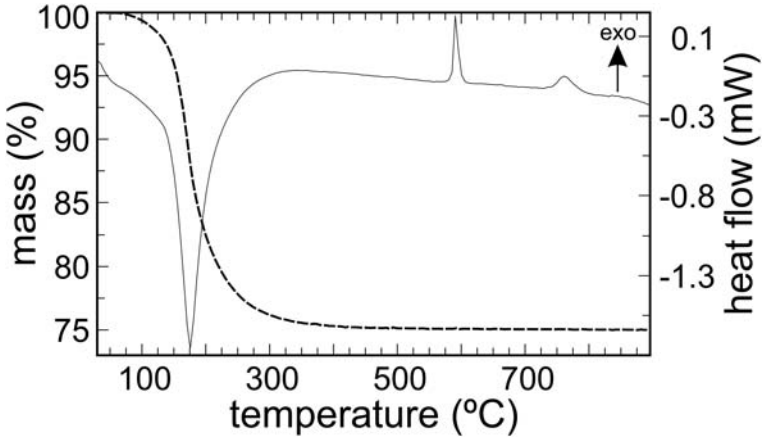

FIG. 6. Results of the thermogravimetric analysis for koninckite.

https://doi.org/10.1180/minmag.2015.079.5.10 Published online by Cambridge University Press

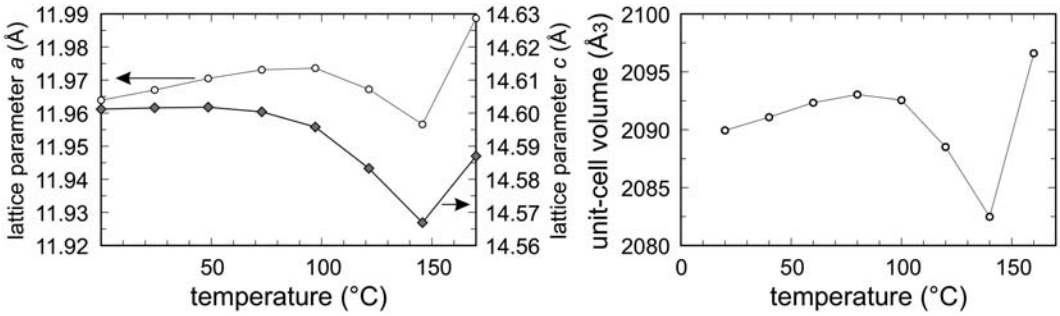

FIG. 7. The evolution of the unit-cell volume with temperature derived from the variable-temperature powder XRD data. The line between the points serves only as a guide to the eye. The uncertainties are smaller than the symbols.

TABLE 5. Lattice parameters of koninckite as a function of temperature. The variations are shown graphically in Fig. 6.

T (°C)	a (Å)	c (Å)	V (Å^3)
20	11.9639(6)	14.6012(8)	2089.94(19)
40	11.9670(6)	14.6016(8)	2091.08(18)
60	11.9705(6)	14.6018(7)	2092.33(18)
80	11.9731(6)	14.6004(7)	2093.04(17)
100	11.9736(5)	14.5958(7)	2092.55(17)
120	11.9672(5)	14.5833(7)	2088.51(16)
140	11.9566(6)	14.5669(8)	2082.48(19)
160	11.9887(21)	14.5870(27)	2096.60(60)

similar to koninckite. Synthetic Fe-phosphate zeolites play a special role because of the possibility of combining their magnetic properties and their capability to serve as a molecular sieve (e.g. Maspoch *et al.*, 2007). Many Fe phosphates are synthesized by templating the hydrothermally prepared structures with organic molecules (Lii *et al.*, 1998), either in aqueous or non-aqueous solvents. A significant amount of work was invested into the ferrofluorophosphates (e.g. Cavellec *et al.*, 1996; Keates *et al.*, 2013).

Parageneses and formation of koninckite

Table 6 presents, to our best knowledge, a complete overview of the sites and parageneses involving koninckite and documents the secondary origin of this mineral. The primary nature of the occurrence in Japan can be questioned, given the lack of geological and geochemical information about the volume of rocks that interact with the aqueous fluids in the hot springs. It could be suggested that these low-temperature fluids are causing the alteration and transport of an Fe-enriched ore body in an environment with abundant phosphate. The surficial manifestation of these processes is then the 'primary' precipitation of koninckite. This overview also shows that koninckite is one of the less abundant phases at most of the sites, perhaps with the exception of Kociha (Rimavská Sobota, Slovakia).

In the present study, we have combined experimental XRD and first-principles computations to derive a complete structural model for koninckite. The space group and crystallographic locations of the heavy components (Fe, P and O) could be resolved within the experimental observations. The DFT computed $FePO_4{\cdot}2H_2O$ equilibrium structure without extra-framework water is similar to our experimental X-ray observations, suggesting that extra-framework water has only a small effect on the stability and the crystal chemistry of the framework. The comparison of the equilibrium

https://doi.org/10.1180/minmag.2015.079.5.10 Published online by Cambridge University Press

TABLE 6. A summary of the occurrences of koninckite, with notes on the geological environment of each occurrence and a list of the associated minerals.

Geological environment	Koninckite occurrence and properties	Associated species	Locality and references
Hot-spring precipitates; hot springs reported to be still active in 1959 but the mining of Fe ores ceased; no details on the temperature and water properties in the hot springs	Koninckite considered to be primary here	Fe oxides ('limonite') and jarosite [$KFe_3(SO_4)_2(OH)_6$]	Suwa mine, Japan (Sakurai *et al.*, 1987)
Deeply weathered tectonic zone in graphitic phyllites rich in pyrite and phosphatic sandstones enriched in U and V	White or pinkish-white botryoidal aggregates or radial druses of minute crystals on quartz crystals (Figs 1*b*,*c*,*d*)	Evansite [$\sim Al_3(PO_4)(OH)_6 \cdot 6H_2O$], vashegyite [$\sim Al_6(PO_4)_5(OH)_3 \cdot 23H_2O$] and volborthite [$Cu_3V_2O_7(OH)_2 \cdot 2H_2O$]; all minerals found in masses of Fe oxides and Fe phosphates	Kociha, Rimavská Sobota, Slovakia (Novák *et al.*, 2003)
Gossan developed by weathering of pyrite in the host rocks rich in cryptocrystalline apatite	Masses and veinlets	Destinezite [$Fe_2(PO_4)(SO_4)(OH) \cdot 6H_2O$] and delvauxite [$CaFe_4(PO_4,SO_4)_2(OH)_8 \cdot 4–6H_2O$]	Litošice, Czech Republic (Jirásek, 2005)
Fractures of black shales; it is assumed that koninckite crystallized by the interaction of Fe-enriched aqueous solutions with phosphate-rich fossils (conodonts)	Radial aggregates	Hexahydrite ($MgSO_4 \cdot 6H_2O$), calcite, aragonite, gypsum and rozenite ($FeSO_4 \cdot 4H_2O$)	Oberbuchach, Austria (Puttner, 1997)
Weathering product of pyrite-bearing aluminous shales; it could be assumed, although not stated explicitly, that koninckite is linked to the 'glauconite-phosphatic' facies of the shales that contain common phosphate-rich oolites		Common weathering products are Fe-Mn oxides and jarosite, rare ones are smithsonite ($ZnCO_3$), koninckite, vivianite [$Fe_3(PO_4)_2 \cdot 8H_2O$], torbernite [$Cu(UO_2)_2(PO_4)_2 \cdot 8–12H_2O$], melanterite ($FeSO_4 \cdot 7H_2O$) and epsomite ($MgSO_4 \cdot 7H_2O$)	Russia (Altgauzen and Kuznecova, 1971)
Uraniferous laterites dominated by goethite, hematite and gibbsite, with minor quartz, kaolinite and metavariscite ($AlPO_4 \cdot 2H_2O$)		Barite, apatite, variscite ($AlPO_4 \cdot 2H_2O$) and a variety of U phosphates	Paraná basin, Brazil (Leonardos *et al.*, 1987).
Supergene alteration of apatite	Pinkish-white crusts and radial aggregates		Pollone mine, Italy (Senesi, 2000)
Cavities in kyanite gneisses	Pinkish-red radial aggregates	Woodhouseite {$CaAl_3[(OH)_6(SO_4)(PO_4)]$}	Untersulzbachtal, Austria (Burgsteiner, 1997 in Leute, 1999)
Fractures of feldspars and diopside in apatite-enriched fenitic rocks		Weathered pyrite	Kola Penninsula, Russia, (Ivanyuk and Yakovenchuk, 1997)

Weathering product of triphylite ($LiFePO_4$) in a pegmatite	Earthy masses		Turkestan ridge, former Soviet Union (Beus, 1950)
Fractures in pyrite-rich shales	Beige radial aggregates	Phosphosiderite ($FePO_4{\cdot}2H_2O$), gypsum, crandallite [$CaAl_3(PO_4)_2(OH)_5{\cdot}H_2O$] and perhamite [$(Ca_3Al_7(SiO_4)_3(PO_4)_4(OH)_3{\cdot}16.5H_2O$]	Hardtkopf, Sauerland, Germany (Blaß and Graf, 1995)
Fractures in radiolarites	Pinkish-white radial aggregates	Strunzite ($MnFe_2(PO_4)_2(OH)_2{\cdot}6H_2O$), beraunite ($Fe^{2+}Fe^{3+}_5(PO_4)_4(OH)_5{\cdot}4H_2O$) and diadochite [$Fe_2(PO_4)(SO_4)(OH){\cdot}6H_2O$]	Arnsberg (Weiß *et al.*, 1990)
	Small brown nodules	Jarosite	Montcada mountain near Barcelona, Spain (Riba, 1997)
Shales		Ferric and aluminous phosphates	Nekészeny and Nekészeny-Dédestapolcsány, Hungary (Szakáll and Gatter, 1993)

structures shows very good agreement within the limitations of experiment and theory and corroborates the weak effect of extra-framework water on the crystal chemistry in $FePO_4{\cdot}3H_2O$. The anomalously short Fe–O bond length derived from the experimental data is not supported by the computations and may be viewed as an artifact of the powder diffraction data. Furthermore, the computations predict that koninckite is an antiferromagnetic semiconductor at least at low temperatures, similar to FeO (Mazin *et al.*, 1998; Schrön *et al.*, 2012). The computations show that extra-framework water uptake in $FePO_4{\cdot}2H_2O$ is exothermic at least up to one H_2O molecule per formula unit, consistent with the chemical formula, $FePO_4{\cdot}3H_2O$. However, the actual amount of extra-framework water present is not only controlled by thermodynamics but also by kinetics, an effect that was not included in our study. The temperature dependent XRD shows that koninckite collapses to an X-ray amorphous Fe phosphate above 160–180°C. Our TGA and DFT computations suggest that the loss of long range order is probably induced by the facile removal of framework and extra-framework H_2O.

Acknowledgements

The authors thank Peter Leverett and Anthony Kampf for thoughtful reviews. J. Jirásek (Univ. Ostrava) is thanked for providing the literature on koninckite, some of it difficult to obtain. The ANKA Angströmquelle Karlsruhe is acknowledged for the provision of the beamtime at the SUL-X beamline and S. Doyle is thanked for help during the measurements. B.K. would like to acknowledge computational resources that were made available by the National Science Foundation through XSEDE under grant number DMR TG-110093. The financial support through the post-doc grant of the GAČR 13-31276P for J.P. is also acknowledged.

References

Altgauzen, M.N. and Kuznecova, E.G. (1971) On the nature of the weathering process of pyrite-bearing aluminous shales. *Litologiya i Poleznye Iskopayemiye*, 41–48 [in Russian].

Bengtson, A., Morgan, D. and Becker, U. (2013) Spin state of iron in Fe_3O_4 magnetite and h-Fe_3O_4, *Physical Review B*, **79**, DOI: 10.1103/PhysRevB.87.155141.

Beus, A.A. (1950) Magnesiophillite and mangankoninckite – new minerals from the pegmatites of Turkestan ridge. *Doklady Akademii Nauk SSSR*, **73**, 1267–1269 [in Russian].

https://doi.org/10.1180/minmag.2015.079.5.10 Published online by Cambridge University Press

Blaß, G. and Graf, H.-W. (1995) Mineralogische Neuigkeiten vom Hardtkopf bei Sundern-Linnepe, Sauerland. *Mineralien-Welt*, **6(4)**, 26–27.

Blöchl, P.E. (1994) Projector augmented-wave method. *Physical Review B*, **50**, 17953–17979.

Brown, I.D. (2002) *The Chemical Bond in Inorganic Chemistry.* IUCr Monongraphs in Crystallography **12**. Oxford Science Publications, Oxford, UK.

Brown, I.D. and Shannon, R.D. (1973) Empirical bond-strength – bond-length curves for oxides. *Acta Crystallographica*, **A29**, 266–282.

Cavellec, M., Riou, D., Ninclaus, C., Grenèche, J.-M. and Férey, G. (1996) $[Fe_4(PO_4)_4F_2(H_2O)_3]\cdot[C_6H_{14}N_2]$ or ULM-12, the first magnetic ferric phosphate with an open structure: Hydrothermal synthesis, structure, and magnetic properties. *Zeolites*, **17**, 250–260.

Cesàro, G. (1884) Sur la Koninckite, nouveau phosphate ferrique hydraté. *Annales de la Société géologique de Belgique*, **11**, 247–257.

Dudarev, S.L., Botton, G.A., Savrasov, S.Y., Humphreys, C.J. and Sutton, A.P. (1998) Electron-energy-loss spectra and the structural stability of nickel oxide: An LSDA+U study. *Physical Review B*, **57**, 1505–1509.

Eventoff, W., Martin, R. and Peacor, D.R. (1972) The crystal structure of heterosite. *American Mineralogist*, **57**, 45–51.

Fanfani, L. and Zanazzi, P.F. (1967) The crystal structure of beraunite. *Acta Crystallographica*, **22**, 173–181.

Holzwarth, N.A.W., Matthews, G.E., Dunning, R.B., Tackett, A.R. and Zeng, Y. (1997) Comparison of the projector augmented-wave, pseudopotential, and linearized augmented-plane-wave formalisms for density-functional calculations of solids. *Physical Review B*, **55**, 2005–2017.

Huminicki, D.M.C. and Hawthorne, F.C. (2002) The crystal chemistry of the phosphate minerals. Pp. 123–253 in: Phosphates (M.L. Kohn, J. Rakovan and J.M. Hughes, editors). *Reviews in Mineralogy and Geochemistry*, **48**. Mineralogical Society of America and the Geochemical Society, Chantilly, Virginia, USA.

Ivanyuk, G.Yu. and Yakovenchuk, V.N. (1997) *Minerals of the Kovdor Massif.* RAS Kola Science Center Publishing, Apatity, Russia, 116 pp.

Jirásek, J. (2005) A find of koninckite near Litošice and its comparison with other world occurrences. *Bulletin mineralogicko-petrografického oddělení Národního muzea v Praze*, **269**, 132–137 [in Czech].

Keates, A.C., Armstrong, J.A. and Weller, M.T. (2013) Iron fluorophosphates. *Dalton Transactions*, **42**, 10715–10724.

Kniep, R. and Mootz, D. (1973) Metavariscite – a redetermination of its crystal structure. *Acta Crystallographica*, **B29**, 2292–2294.

Kresse, G. and Furthmüller, J. (1996*a*) Efficiency of ab-initio total energy calculations for metals and semiconductors using a plane-wave basis set. *Computational Materials Science*, **6**, 15–50.

Kresse, G. and Furthmüller, J. (1996*b*) Efficient iterative schemes for ab initio total-energy calculations using a plane-wave basis set. *Physical Review B*, **54**, 11169–11186.

Kresse, G. and Joubert, D. (1999) From ultrasoft pseudopotentials to the projector augmented-wave method. *Physical Review B*, **59**, 1758–1775.

Leonardos, O.H., Fernandes, S.M., Fyfe, W.S. and Powell, M. (1987) The micro-chemistry of uraniferous laterites from Brazil: A natural example of inorganic chromatography. *Chemical Geology*, **60**, 111–119.

Leute, M.A. (1999) Mineralogische Neuigkeiten aus Österreich. *Mineralien-Welt*, **10(5)**, 26–36.

Lii, K.-H., Huang, Y.-F., Zima, V., Huang, C.-Y., Lin, H. M., Jiang, Y.-C., Liao, F.-L. and Wang, S.-L. (1998) Syntheses and structures of organically templated iron phosphates. *Chemistry of Materials*, **10**, 2599–2609.

Majzlan, J. and Kiefer, B. (2006) An X-ray- and neutron-diffraction study of synthetic ferricopiapite, $Fe_{14/3}(SO_4)_6(OD,OH)_2(D_2O,H_2O)_{20}$, and ab initio calculations on the structure of magnesiocopiapite, $MgFe_4(SO_4)_6(OH)_2(H_2O)_{20}$. *The Canadian Mineralogist*, **44**, 1227–237.

Majzlan, J., Đorđević, T., Kolitsch, U. and Schefer, J. (2010) Hydrogen bonding in coquimbite, nominally $Fe_2(SO_4)_3\cdot 9H_2O$, and the relationship between coquimbite and paracoquimbite. *Mineralogy and Petrology*, **100**, 241–248.

Maspoch, D., Ruiz-Molina, D. and Veciana, J. (2007) Old materials with new tricks: multifunctional open-framework materials. *Chemical Society Reviews*, **36**, 770–818.

Mazin, I.I., Fei, Y.W., Downs, R. and Cohen, R. (1998) Possible polytypism in FeO at high pressures. *American Mineralalogist*, **83**, 451–457.

Methfessel, M. and Paxton, A.T. (1989) High-precision sampling for Brillouin-zone integration in metals. *Physical Review B*, **40**, 3616–3621.

Michel, F.M., Hosein, H-A., Hausner, D.B., Debnath, S., Parise, J.B. and Strongin, D.R. (2010) Reactivity of ferritin and the structure of ferritin-derived ferrihydrite. *Biochimica et Biophysica Acta*, **1800**, 871–885.

Moore, P.B. and Shen, J. (1983) An X-ray structural study of cacoxenite, a mineral phosphate. *Nature*, **306**, 356–358.

Moore, P.B. and Kampf, A.R. (1992) Beraunite: refinement, comparative crystal chemistry, and selected bond valences. *Zeitschrift für Kristallographie*, **201**, 263–281.

Novák, F., Pauliš, P., Ševců, J., Kopista, J. and Zeman, M. (2003) Koninckite, evansite, vashegyite, and volborthite from Kociha near Rimavská Sobota (Slovakia). *Bulletin mineralogicko-petrografického oddělení Národního muzea v Praze*, **11**, 159–166 [in Czech].

https://doi.org/10.1180/minmag.2015.079.5.10 Published online by Cambridge University Press

Oszlányi, G. and Sütő, A. (2004) Ab initio structure solution by charge flipping. *Acta Crystallographica A*, **60**, 134–141.

Oszlányi, G. and Sütő, A. (2008) The charge flipping algorithm. *Acta Crystallographica A*, **64**, 123–134.

Palatinus, L. (2013) The charge flipping algorithm in crystallography. *Acta Crystallographica B*, **69**, 1–16.

Palatinus, L. and Chapuis, G. (2007) Superflip – a computer program for the solution of crystal structures by charge flipping in arbitrary dimensions. *Journal of Applied Crystallography*, **40**, 451–456.

Palatinus, L. and van der Lee, A. (2008) Symmetry determination following structure solution in *P*1. *Journal of Applied Crystallography*, **41**, 975–984.

Perdew, J.P., Burke, K. and Ernzerhof, M. (1996) Generalized gradient approximation made simple. *Physical Review Letters*, **77**, 3865–3868.

Petříček, V., Dušek, M. and Palatinus, L. (2006) *Jana2006. The crystallographic computing system*. Institute of Physics, Praha, Czech Republic.

Petříček, V., Dušek, M. and Palatinus, L. (2014) Crystallographic Computing System Jana 2006: General features. *Zeitschrift für Kristallographie*, **229**, 345–352.

Punkkinen, M.P.J., Kokko, K., Hergert, W. and Vayrynen, I. J. (1999) Fe_2O_3 within the LSDA+U approach. *Journal of Physics – Condensed Matter*, **11**, 2341–2349.

Puttner, M. (1997) Das seltene Phosphatmineral Koninckit in einer Mineralisation von Geo-Trial bei Oberbuchach, Karnische Alpen (Kärnten). *Aufschluss*, **48**, 317–320.

Riba, J.R. (1997) El Turó de Montcada (Montcada i Reixac, Vallès Occidental). Història, Mineria i Mineralogia. *Revista de Minerals Mineralogistes de Catalunya*, **12**, 34–55 [in Catalan].

Robinson, K., Gibbs, G.V. and Ribbe, P.H. (1971) Quadratic elongation: a quantitative measure of distortion in coordination polyhedra. *Science*, **172**, 567–570.

Rollmann, G., Rohrbach, A., Entel, P., Hafner, J. (2004) First-principles calculation of the structure and magnetic phases of hematite. *Physical Review B*, **69**, 165107.

Sakurai, K., Matsubara, S. and Kato, A. (1987) Koninckite from Suwa Mine, Chino City, Nagano Prefecture, Japan. *Bulletin of the National Science Museum, Series C (Geology & Paleontology)*, **13**, 149–156.

Schrön, A., Rödl, C. and Bechstedt, F. (2012) Crystalline and magnetic anisotropy of the 3d-transition metal monooxides MnO, FeO, CoO, and NiO. *Physical Review B*, **86**, 115134.

Senesi, F. (2000) Koninckite e altri fosfati della miniera del Pollone (Valdicastello Carducci, Lucca). *Rivista Mineralogica Italiana*, **1**, 46–48.

Shirley, R. (2000). *The CRYSFIRE System for Automatic Powder Indexing: Users Manual.* The Lattice Press, Guildford, Surrey, England.

Szakáll, S. and Gatter, I. (1993) *Mineral Species of Hungary.* Fair System Kft., Miskolc, Hungary [p. 64–65, in Hungarian].

van Tassel, R. (1968) Données cristallographiques sur la koninckite. *Bulletin Société Français de Minéralogie et de Cristallographie*, **91**, 487–489.

Voegelin, A., Kaegi, R., Frommer, J., Vantelon, D. and Hug, S.J. (2010) Effect of P, Si, and Ca on Fe(III)-precipitates formed in aerated Fe(II) and As(III) containing water studied by X-ray absorption spectroscopy. *Geochimica et Cosmochimica Acta*, **74**, 164–186.

Vosko, S.H., Wilk, L. and Nusair, M. (1980) Accurate spin-dependent electron liquid correlation energies for local spin-density calculations. *Canadian Journal of Physics*, **58**, 1200–1211.

Wang, X., Liu, F., Tan, W., Li, W., Feng, X. and Sparks, D.L. (2013) Characteristics of phosphate adsorption-desorption onto ferrihydrite: Comparison with well-crystalline Fe (hydr)oxides. *Soil Science*, **178**, 1–11.

Weiß, S. (1990) *Mineralfundstellen Atlas Deutschland West.* Christian Weise Verlag GmbH, München, Germany.

Wenzel, M.J. and Steinle-Neumann, G. (2007) Nonequivalence of the octahedral sites of cubic Fe_3O_4 magnetite. *Physical Review B*, **75**, 214430.

https://doi.org/10.1180/minmag.2015.079.5.10 Published online by Cambridge University Press